Three-dimensional unsteady modeling analysis of silicon transport in melt during Cz growth of $Ge_{1-x}Si_x$ bulk crystals

O.V. Smirnova[a], V.V. Kalaev[b],*, Yu.N. Makarov[b], N.V. Abrosimov[c],
H. Riemann[c], V.N. Kurlov[d]

[a]Soft-Impact Ltd., 27 Engels av., P.O. Box 83, 194156, St. Petersburg, Russia
[b]STR GmbH, P.O. Box 1207, D-91002 Erlangen, Germany
[c]Institute for Crystal Growth, Max-Born-Str.2, D-12489, Berlin, Germany
[d]Institute of Solid State Physics of RAS, 142432 Chernogolovka, Russia

Available online 17 January 2007

Abstract

Si transport in the melt during Czochralski (Cz) growth of $Ge_{1-x}Si_x$ bulk crystals has been simulated within a 3D unsteady approach using two models of Si sources. The effect of the rod number on Si supply to the crystallization front is discussed. The crystallization front geometry is computed taking into account crystallization temperature varying with Si concentration. The predicted geometry is compared with experimental data. To study the effect of 3D unsteady melt motion, the results are compared with 2D axisymmetric computations of Si transport.
© 2006 Elsevier B.V. All rights reserved.

1. Introduction

The growing interest for $Ge_{1-x}Si_x$ single crystals (such as mosaic crystals for γ-ray telescopes [1]) requires the development of a reliable growth technique and adjusted growth conditions. A successful technique in this case is the Czochralski (Cz) method. However, seeding for single-crystal growth is related to a number of difficulties due to the difference in properties of silicon and germanium and also because Si segregation coefficient in germanium is greater than 1. It is hard to use a Ge seed for growth form a $Ge_{1-x}Si_x$ melt because the germanium melting temperature is the smallest in the Si–Ge system and it is difficult to avoid seed melting. Using of a silicon seed often results in the growth of polycrystals but this approach was successfully used for growing crystals of a small diameter [2]. It is well known that the Cz method with continuous feeding allows avoiding difficulties at seeding because the growth starts from Ge melt, using a Ge seed [3,4]. Dissolving Si rods provides the necessary silicon concentration in the melt and compensates a decrease of silicon concentration due to segregation. The obtained crystals have a nearly constant composition or a certain axial gradient of the composition. Therefore, the control of the silicon transport from solving rods to the crystallization front and its incorporation into the front is of high importance.

There is a wide experience in simulation of impurity transport during single crystal growth. For example, oxygen transport in the melt during Cz growth of Si crystals is profoundly studied [5–7]. There are works on carbon transport in the melt [8] during GaAs VCz growth, on gallium transport during vertical Bridgman growth of Ga-doped germanium [9] and etc. Kitashima et al. [10] numerically analyzed the transport of raw material supplied onto the melt surface during a double–crucible Cz growth of lithium niobate with continuous charging. The paper of Minakuchi [11] presents computations accounting for the 3D transport of silicon in the melt during the growth of Si_xGe_{x-1} crystals by the float-zone

*Corresponding author. Tel.: +49 1728387236; fax: +49 9131972398.
E-mail address: vladimir.kalaev@strgmbh.de (V.V. Kalaev).

technique. However, the Si transport during $Ge_{1-x}Si_x$ crystal growth is still poorly studied. The aim of our work is to analyze numerically the Si transport in the melt during Cz $Ge_{1-x}Si_x$ growth with continuous feeding. We have applied a 3D unsteady approach considering silicon as a passive impurity.

2. Experimental procedure

$Ge_{1-x}Si_x$ crystals with $x = 0.02$ in the cylindrical part were grown by the Cz method with continuous feeding [3,4]. In this technique, the crucible is filled with pure germanium and Ge crystal growth on a Ge seed is started after charge melting. When the growth becomes stable and the crystal tends to expand, three silicon rods with a diameter of 7 mm are dipped into the melt. The rod solving is controlled by the crucible moving and calculated to obtain 2 at% of Si in beginning of the cylindrical part of the crystal. To compare with computations, we selected the crystal with a diameter of 33 mm and a length of 110 mm, presented in Fig. 1. The crystal and crucible rotation rates were 15–10 rpm, respectively. The pulling rate during the growth of the cylindrical part was about 6 mm/h.

3. Modeling approach

The 2D/3D model successfully applied for the simulation of the $Si_{1-x}Ge_x$ melt flow and heat transfer [12] was extended to describe the Si transport in the $Ge_{1-x}Si_x$ melt. The approach has two steps: (i) axisymmetric global heat transfer computation and (ii) 3D modeling of heat and mass transport in the crystallization zone. The axisymmetric global heat computation considers radiative and conductive heat transfer in the whole facility. Further detailed steps of 3D analysis of the crystallization zone utilizes the radiative and conductive heat fluxes obtained in the global heat computation to formulate temperature boundary conditions along the outer boundaries of the crystal, crucible and melt free surface. Melt convection is considered by the LES (large eddy simulation) method [13]. Besides, additional 2D computations for the crystallization zone are provided within the 2D Reynolds-averaged approach using a modification of the Chien turbulence model [14]. The Navier–Stokes equations written for an incompressible flow with the Boussinesq approximation of buoyancy are used in both cases.

For a correction of the crystallization front geometry, we applied an algorithm with grid reconstruction in the adjoining blocks. The melt–crystal interface is computed to provide the uniform axial component distribution of the time-averaged crystallization rate over the front.

The extended approach accounts for diffusive and convective transport of Si in the melt, which is described by the following equation:

$$\frac{\partial(\rho_{melt} C_{melt})}{\partial t} + \nabla \cdot (\rho_{melt} \vec{u} C_{melt}) = \nabla \cdot (D \nabla C_{melt}). \quad (1)$$

Here, ρ_{melt} is the melt density, $\vec{u}$ is the melt velocity, C_{melt} is the Si mass fraction in the melt, and D is the Si dynamic diffusivity.

A part of the melt free surface is considered as a Si source. The following boundary conditions are set at the melt–crystal interface to consider silicon release from the melt:

$$\rho_{melt} D \frac{\partial C_{melt}}{\partial n} = -\rho_{cryst} V_{cr}(1 - k_{Si}) C_{melt}, \quad (2)$$

where ρ_{melt} and ρ_{cryst} are the melt and crystal densities, D is the Si diffusion coefficient in the Ge melt, C_{melt} is the Si mass fraction in the melt, V_{cr} is the crystallization rate, $k_{Si} = 3$ is the Si distribution coefficient in the Ge melt, n is the normal direction to the crystallization front.

The source condition at melt–rod boundaries is formulated in the following way:

$$\rho_{melt} D \frac{\partial C_{melt}}{\partial n} = \rho_{rod} V_{sol} \beta K, \quad (3)$$

where ρ_{rod} is the rod density, V_{sol} is the dissolution rate of the rod, K is the correction factor found to provide about 0.7 at% Si in the melt at the triple point, which corresponds to 2 at% of Si in the crystal. Two ways of the Si source simulation are applied: (i) a simplified method, when the source is considered to be a ring with the width equal to the rod diameter (the ring model) and (ii) an accurate approach

Fig. 1. The $Ge_{1-x}Si_x$ crystal grown by the Cz method with continuous Si feeding of the melt.

Table 1
Thermal conductivity λ, density ρ and emissivity ε of $Ge_{1-x}Si_x$ crystals and melts

Conductivity (W m^{-1} K^{-1})	
Crystal	$\lambda_{GeSi} = \lambda_{Ge}(1 - 5x)$ with $\lambda_{Ge} = 17$ ($T = 1000$ K) [16]
Melt	$\lambda_{GeSi} = \lambda_{Ge}(1 - x) + \lambda_{Si}x$ with $\lambda_{Si} = 66.5$, $\lambda_{Ge} = 39$ ($T = T_{melting}$) [17]
Density (kg/m^3)	
Crystal	$\rho_{GeSi} = \rho_{Ge}(1 - x) + \rho_{Si}x$ with $\rho_{Si} = 2300$, $\rho_{Ge} = 5260$
Melt	$\rho_{GeSi} = \rho_{Ge}(1 - x) + \rho_{Si}x$ with $\rho_{Si} = 3194 - 0.3701 \cdot T$, $\rho_{Ge} = 6170 - 0.442 \cdot T$ [18]
Emissivity	
Crystal	$\varepsilon_{GeSi} = \varepsilon_{Ge} = 0.55$ [19]
Melt	$\varepsilon_{GeSi} = \varepsilon_{Ge} = 0.2$ [19]

with the three separate Si/Ge$_{1-x}$Si$_x$ interfaces as in reality. Within the ring model, the supplied silicon mass flux should be distributed over a ring and parameter β in Eq. (3) is taken to be ($3S_{rod}/S_{ring}$), where S_{rod} is the rod cross-section area, S_{ring} is the area of the ring. If the Si source is considered as three separate areas, coefficient β equal to 1. The zero flux condition is used at other boundaries such as the free surface and the melt–crucible interface.

Following Ref. [10], the crystallization temperature depends on the Si concentration in the crystal as this given by,

$$T_{cryst} = 1412 - 738(1 - C_{cryst}) + 263(1 - C_{cryst})^2 + 273(K),$$
(4)

which is accounted for in the crystallization front geometry computation, as well as in the boundary conditions at the front. Further material parameters of the melt and crystal used in the modeling are presented in Table 1.
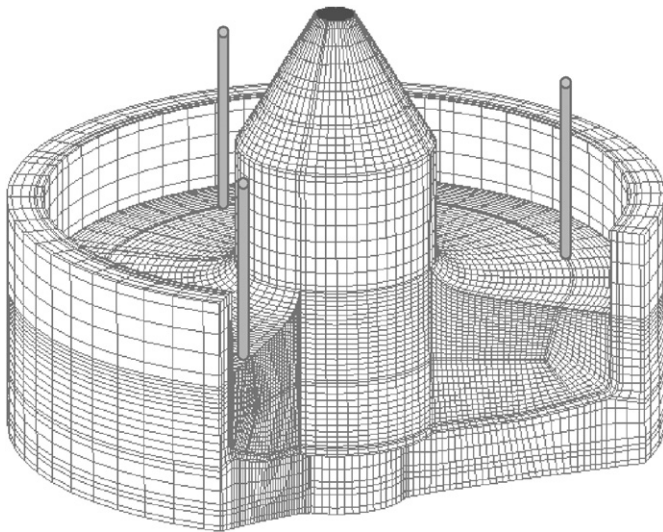
Fig. 2. The computational grid used for the 3D computations in the crystallization zone; the three Si rods are shown schematically.

The CGSim (Crystal Growth Simulator) program package (www.semitech.us) was used for all computations. The fourth and second approximation orders were applied for convective and diffusive terms, respectively. A time step of 0.5 s was chosen for unsteady calculations to resolve unsteady transitions of different scales.

4. Results and discussion

We considered the growth stage corresponding to crystal height 20 mm. Axisymmetric global heat computations were done using a combined grid containing 8000 finite volumes [15]. The power of the heater was slightly adjusted to provide the desired crystallization rate.

A typical 3D computational grid of the crystallization zone including the melt, crystal and crucible is shown in Fig. 2. It contains about 110,000 cells. After getting the required crystallization rate about 2000 s are needed to obtain a time-averaged melt velocity distribution which does not change with increase of the averaging period.

The averaged in time Si distributions at the melt-free surface obtained in the 3D computations within both source models are presented in Fig. 3. The maximum values of 0.716 and 0.727 at% are computed with the ring model and the model with separate sources, respectively. One can see that there is a ring with a high Si concentration in both cases. It can be explained by involving Si in the rotary melt motion produced by the crucible rotation. So it is possible to simulate Si rods reasonably by both three real size sources and by a ring source at these growth conditions. Note that the correction factor K in formula (3) is found to be of 1.1 for both approaches, which proves the model applicability. The small deviation of this factor from 1 can be explained by the fact that the rod solution front slowly goes up from the melt-free surface during growth. But we suggest, for simplicity, that the solution front coincides with the melt-free surface. So the rod solution rate may differ from the averaged value of 0.35 mm/h used in the computations.
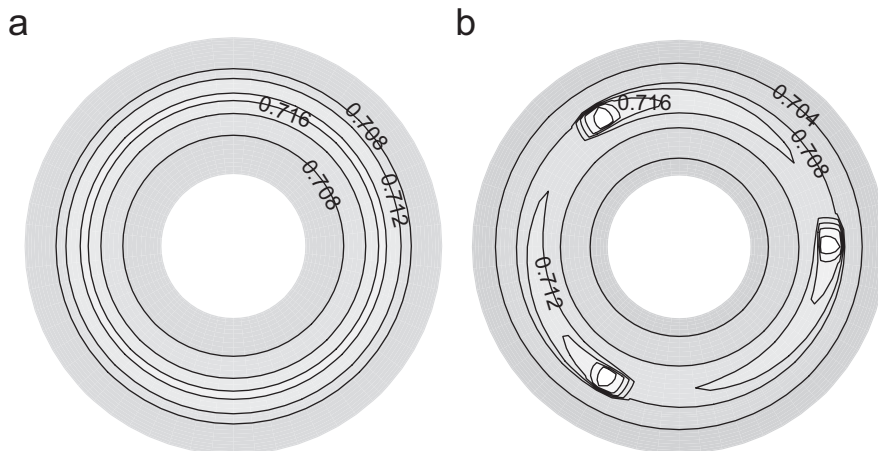
Fig. 3. The time-averaged distributions of the Si concentration (atomic fraction in %) over the free melt surface computed within the ring model (left) and the model with the separate sources (right).
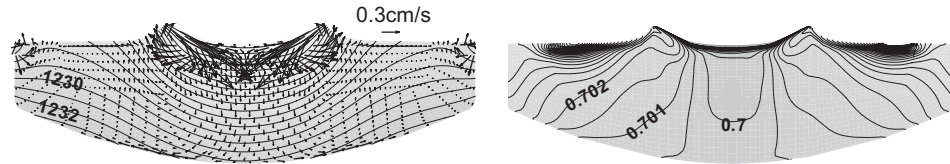
Fig. 4. The time-averaged temperature distributions and melt flow patterns (left) and the averaged Si distribution (right) obtained in the 3D computations within the model with separate sources.
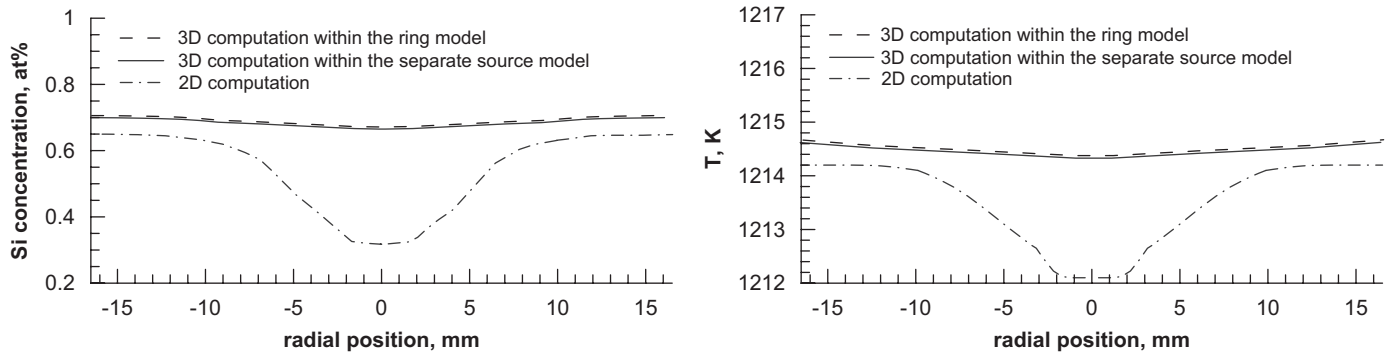
Fig. 5. The Si concentration distributions (left) and the melting temperature distribution (right) along the crystallization interface obtained in the 3D and 2D computations.

It was found that the melt flow is turbulent and consists of continuously reconstructed vortexes providing active mass exchange in the melt. The time-averaged flow pattern and the temperature distributions are demonstrated in Fig. 4 (left). It is obvious that the flow has no dominating downward jet. The temperature minimum and maximum are 996 and 1250 K, respectively. The averaged Si concentration obtained with the model with separate sources is shown in Fig. 4 (right). One can see a rod as an area with the highest Si concentration (0.727 at%) at the melt surface in the right part of the cross-section. In the left part, the area with a quite large concentration value is the ring obtained due to the crucible rotation. The minimum value of the melt silicon concentration is found to be 0.67 at%.

The Si concentration and melting temperature distributions along the crystallization front obtained in the 3D computations with both models are shown in Fig. 5. It is obvious that they are quite close, which can be explained by formation of the high Si concentration ring in the computations with three rods. So the computed melt–crystal interface shapes are practically identical. The shape is in a good agreement with the experiment data, which demonstrates that the model predicts the crystal growth fairly well (Fig. 6).

The presence of the high Si concentration ring suggests an idea to make a 2D computation, which does not require such high computational resources as the 3D approach and takes a short time to obtain a result. So the 2D computations of heat and mass transport in the crystallization zone were done as described above and the results are presented in Figs. 5–7. The melt temperature is in the range between 998 and 1248 K. The minimum silicon
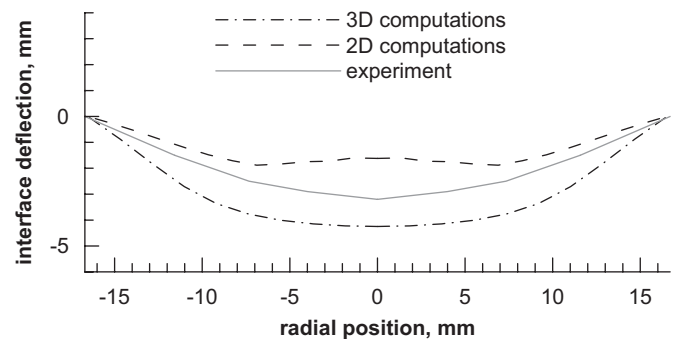
Fig. 6. Comparison of the crystallization front shape obtained in the 2D and 3D computations and the experimental geometry.

concentration is obtained to be at the melt interface center and equal to 0.35 at%. Comparing the averaged 3D flow and the pattern obtained in the 2D computations, one can see that there is a strong jet under the crystal in the 2D results (Fig. 7). The jet carries off silicon, which results in the overestimation of the concentration gradient along the front (Fig. 5 (left)). This leads to a significant variation of the melting temperature (Fig. 5 (right)) and, therefore, to the waved interface geometry with underestimated deflection (Fig. 6).

5. Conclusions

3D computations of Si transport were made within two approaches: a ring model and a model with separate Si sources of the experimental size and position.

Both 3D approaches predict nearly the same concentration distribution along the interface because of a quite high
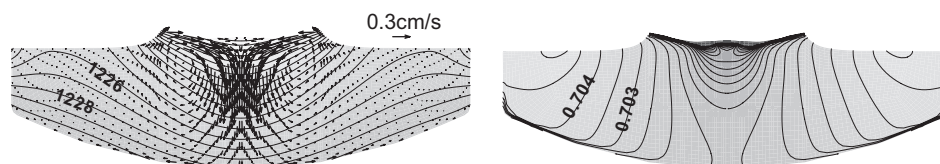
Fig. 7. The temperature distributions and melt flow patters (left) and the Si distribution (right) obtained in the 2D computations.

crucible rotation rate resulting in rotating motion on the melt free surface. The flow involves silicon in the motion, and the ring with a high Si concentration appears on the melt surface. The identical Si distributions result in nearly the same melting temperature and, therefore, in the same shape of the crystallization front, which is close to the experimental data. The obtained Si concentration distribution at the melt surface shows that when the number of rods is greater than three one obtain the same result. In this crystal growth case, we might suggest that even using a single Si rod is enough to get an axisymmetric concentration profile across the crystallization front. However, the effect of the rod number may be really three dimensional and not axisymmetric at a lower crucible rotation rate, which can be studied in a further analysis.

Note that 2D computations overestimate significantly the Si concentration reduction at the axis of rotation due to the strong flow jet carrying off silicon from the crystallization front. Therefore, the melting temperature variation along the interface is overestimated and this results in waves geometry of the crystallization front.

Thus one can conclude that the 3D approach is a promising way to study heat and mass transfer in the melt during Cz growth of $Ge_{1-x}Si_x$ bulk crystals and can be applied as a numerical tool supporting the optimization of crystal growth.

References

[1] H. Halloin, P. von Ballmoos, J. Evrard, G.K. Skinner, N.V. Abrosimov, P. Bastie, G. Di Cocco., M. George, B. Hamelin, P. Jean, J. Knödlseder, Ph. Laporte, C. Badenes, Ph. Laurent, A. Laurens, R.K. Smither, Nucl. Instr. and Meth. A 504 (2003) 120.
[2] I. Yonenaga, Y. Murakami, J. Crystal Growth 191 (1998) 399.
[3] N.V. Abrosimov, S.N. Rossolenko, W. Thieme, A. Gerhardt, W. Schröder, J. Crystal Growth 174 (1997) 182.
[4] N.V. Abrosimov, A. Lüdge, H. Riemann, V.N. Kurlov, D. Borissova, V. Klemm, H. Halloin, P. von Ballmoos, P. Bastie, B. Hamelin, R.K. Smither, J. Crystal Growth 275 (2005) 495.
[5] K. Kakimoto, J. Crystal Growth 230 (2001) 100.
[6] Y.-R. Li, N. Imaishi, Y. Akigama, L. Peng, S.-Y. Wu, T. Tsukada, J. Crystal Growth 266 (2004) 48.
[7] V.V. Kalaev, V.A. Zabelin, Yu.N. Makarov, Solid State Phenom. 82–84 (2002) 41.
[8] E.N. Bystrova, V.V. Kalaev, Yu.N. Makarov, Ch. Frank-Rotsch, M. Neubert, P. Rudolph, J. Crystal Growth 275 (2005) 507.
[9] C.W. Lan, I.F. Lee, B.C. Yeh, J. Crystal Growth 254 (2003) 503.
[10] T. Katashima, L. Liu, K. Kitamura, K. Kakimoto, J. Crystal Growth 266 (2004) 109.
[11] H. Minakuchi, Y. Okano, S. Dost, J. Crystal Growth 266 (2004) 140.
[12] O.V. Smirnova, V.V. Kalaev, Yu.N. Makarov, N.V. Abrosimov, H. Riemann, J. Crystal Growth 266 (2004) 74.
[13] P.R. Spalart, Int. J. Heat Fluid Flow 21 (2000) 252.
[14] K.-Y. Chien, AIAA J. 20 (1982) 33.
[15] O. Smirnova, V. Kalaev, Yu. Makarov, N. Abrosimov, H. Riemann H., in: Sixth International Conference Single Crystal Growth and Heat & Mass Transfer. Obninsk-2005, Proceedings, p. 716.
[16] F. Schäffler, in: Levinshtein, Rumyantsev, Shur Properties of Advanced Semiconductor Materials, (Eds.), 2001.
[17] O. Pätzold, B. Fischer, A. Cröll, Cryst. Res. Technol. 37 (2002) 1058.
[18] H. Nakanishi, K. Nakarato, S. Asaba, K. Abe, S. Maeda, K. Terashima, J. Crystal Growth 191 (1998) 711.
[19] N. van den Bogaert, F. Dupret, J. Crystal Growth 171 (1997) 65.